Theoretical Investigation of Knowles Hydroamination Based on Systematic Exploration of Oxidation/Reduction Pathways for Photoredox-Catalyzed Radical Process

Yu Harabuchi,*[,1,2,3] Hiroki Hayashi,[1,2] Hideaki Takano,[1,2] Tsuyoshi Mita,[1,2] and Satoshi Maeda,*[,1,2,3,4]

[1] Institute for Chemical Reaction Design and Discovery (WPI-ICReDD), Hokkaido University, Kita 21, Nishi 10, Kita-ku, Sapporo, Hokkaido 001-0021, Japan

[2] JST, ERATO Maeda Artificial Intelligence in Chemical Reaction Design and Discovery Project, Kita 10, Nishi 8, Kita-ku, Sapporo, Hokkaido 060-0810, Japan

[3] Department of Chemistry, Faculty of Science, Hokkaido University, Kita 10, Nishi 8, Kita-ku, Sapporo, Hokkaido 060-0810, Japan

[4] Research and Services Division of Materials Data and Integrated System (MaDIS), National Institute for Materials Science (NIMS), Tsukuba, Ibaraki 305-0044, Japan

ABSTRACT: Systematic exploration of reaction paths based on quantum chemical calculations revealed the entire mechanism of Knowles's light-promoted catalytic intramolecular hydroamination *via* radical processes. Bond formation/cleavage competes with single electron transfer (SET) from the catalyst/substrate to substrate/catalyst. All these processes were theoretically described by reactions through transition states in the same electronic state and non-radiative transitions through the seam of crossings (SX) between different electronic states. This study determined the energetically favorable reaction path by combining the reaction path searches and the SX geometry searches, and then discusses the entire reaction mechanism. Such a calculation was achieved by establishing a novel computational approach that represents SET as a non-adiabatic transition between substrate's PESs for different charge states adjusted based on the catalyst's redox potential. Finally, we uncovered the whole picture of the reaction process, in which N atom of the substrate is oxidized by photoredox catalyst *via* SET, the resulting aminium radical is added to alkene, and the hydroamination product is produced after SET process accompanying protonolysis with MeOH. The present calculations showed that the reduction and proton transfer proceed concertedly. Also, in the reduction process, there are SET paths leading to both the product and the reactant, and the redox potentials of the catalyst change the contribution of the SET path leading to the product.

INTRODUCTION

The computational analysis and elucidation of chemical reaction pathways provide important mechanistic insights into organic and biochemical reactions.[1] These quantum chemical calculations could yield the geometries and/or energy relationships among reactants, intermediates, products, and transition states (TSs).[2–5] Conventionally, the calculations are carried out for known chemical processes based on the experimental results or chemist's intuition. Nevertheless, without such "hints" it is very difficult to computationally elucidate plausible frameworks of the reactions. There have been significant progresses in methods that systematically explore the reaction paths, which may be used for reaction estimation toward new methodology development.[6–8]

Theoretical investigations of free-radical transformations have been carried out extensively, and many photochemical reactions involving radical paths have been developed since Nicewicz and MacMillan's study in 2008.[9] A free radical with seven valence electrons that do not satisfy the octet rule is a highly reactive species; it has great potential to promote transformations that are difficult using common ionic transformations. Therefore, precisely calculating the behavior of radical species is highly useful for designing and even predicting new radical transformations to produce fine chemicals, functional molecules, complex molecules, *etc*.

During the last two decades, photoredox catalysis has emerged as a tool to effectively generate radical species under visible light irradiation (**Figure 1a**).[10] In this context, theoretically investigating the whole process of photoredox-catalyzed reactions,[11–15] including bond formation/cleavage events (the radical propagation step) and the single electron transfer (SET) processes between catalysts and substrates/intermediates (the radical initiation/termination step in general) is undoubtedly beneficial for understanding radical reactions (**Figure 1b**). Such calculations would be even more valuable if the reaction outcome could be estimated by computing the energy relationship among the minima and TSs. Although the photoresponses of both organic molecules and transition metal complexes have been widely investigated theoretically, there are several remaining problems. 1) Because photoredox-catalyzed reactions involve a different spin state of each reactant and catalyst (singlet, triplet, *etc*.), calculations must be conducted individually according to each spin state. 2) The SET processes between the photoredox catalyst and substrates/intermediates involve a crossing of potential energy surfaces[16–21] (*i.e*., the seam of crossing (SX)) in the framework of Marcus theory.[22,23] However, most theoretical studies did not explore the SXs, presumably due to either a lack of efficient methods or the relatively large size of catalysts. Instead, researchers just considered the reported redox potentials[9] to assess the feasibility of SET. 3) Several radical paths to afford

the different products often compete with each other.[24] However, estimating the possible by-product paths in a radical reaction is sometimes non-trivial, and thus a thorough exploration of the reaction paths is necessary.
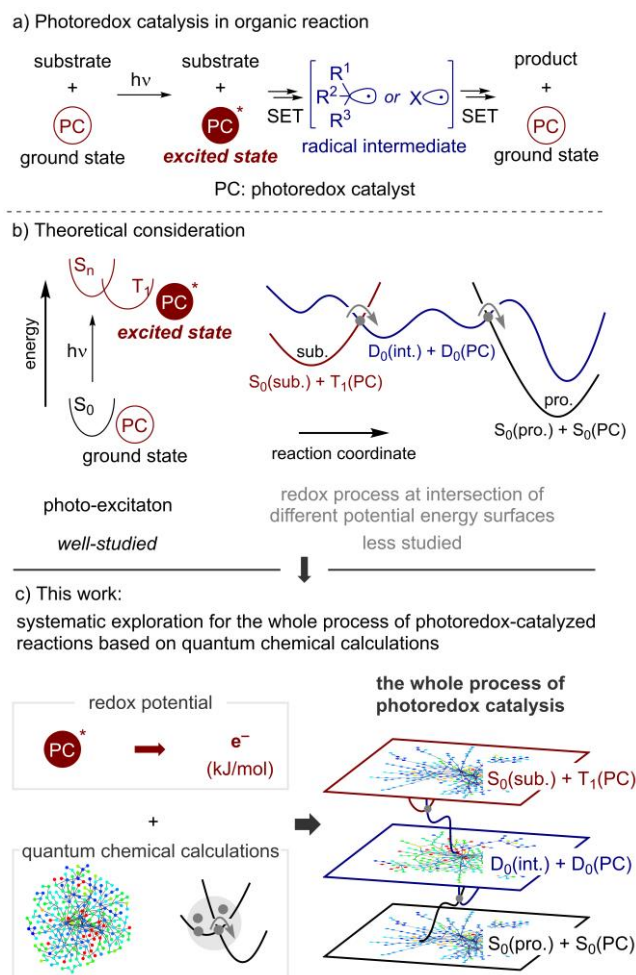

Figure 1. Theoretical investigation of photoredox-catalyzed reactions.

As demonstrated in previous works on chemical reactions in the ground state, automated reaction path search enables the construction of reaction path networks. A reaction path network contains many stable structures (MINs) connected by reaction paths, and kinetic analyses of the network can yield insights into the reaction mechanism.[25,26] A recent advance in reaction path search is predicting reactant candidates starting from the product molecule[27] to develop new reactions.[28] Additionally, in studies of molecular photoresponses, systematic exploring the crossings of potential energy surfaces[29,30] has revealed the mechanism of photoreactions such as, the luminescence of organic molecules,[31] and ligand elimination reactions.[32] Therefore, we hypothesize that combining the reaction path search method with seeking the SXs might overcome the limitations listed above.

Herein, we report a tactical exploration of the whole process of photoredox-catalyzed radical reaction based on quantum chemical calculations (**Figure 1c**). For practical calculations, we used the reported redox potentials[33] of a photoredox catalyst in its excited state instead of the real catalyst structure. This approach reduces the computational cost and thus enables

the construction of multiple reaction path networks of different spin states as well as systematic exploration of the minimum energy SX (MESX) using the artificial force induced reaction (AFIR) method.[34,35] These networks could then be connected in the MESX between the two states. For demonstration, we considered the intramolecular radical hydroamination reported by Knowles *et al.*[36,37] as a model photochemical reaction.

The reported catalytic cycle of Knowles's photoredox hydroamination is shown in **Figure 2a**.[36] The proposed mechanism commences with excitation of the ground state Ir(III) complex ([Ir(ppy)$_2$(dtbbpy)]PF$_6$) by irradiation of blue light. The resulting *Ir(III) species causes oxidation of the substrate to form the corresponding aminium radical intermediate, which undergoes intramolecular radical addition to the alkene moiety. After the one-electron reduction followed by protonation by MeOH (the reaction solvent), the targeted hydroamination product is obtained. The oxidation step of the amine moiety is thought to be at equilibrium and the C–N bond formation is the rate-limiting step, as confirmed by Hammett analysis. From a theoretical point of view, we believe this reaction is divided is categorized into four stages (**Figure 2b**): 1) relaxation of the catalyst to the triplet state (T$_1$) after its photoexcitation to the singlet excited state (S$_n$), 2) a SET process from the substrate to the catalyst (oxidation), 3) C–N bond formation between the aminium radical and alkene (cyclization), and 4) another SET process from the catalyst to the substrate (reduction) followed by protonation. We expect that these processes can be described by a combination of reactions *via* the TSs and non-radiative decays through the SX regions. Therefore, we started by exploring the reaction paths and the decay paths to determine the energetically favorable ones. To achieve this goal, we introduced a new practical approach that allows us to obtain the entire reaction mechanism of the target system using quantum chemical calculations.
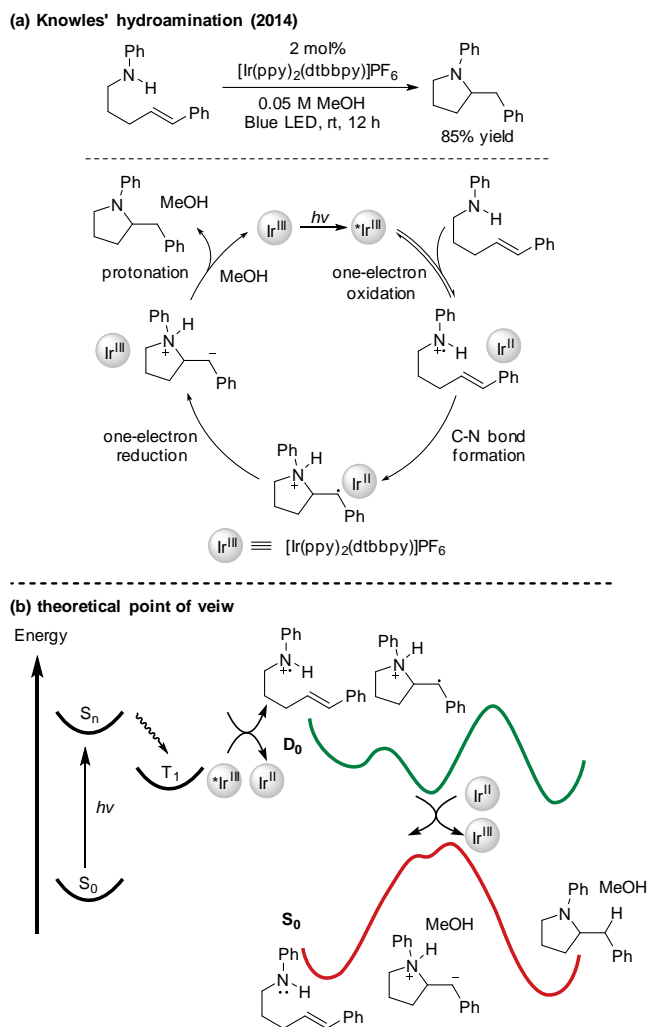
(a) Knowles' hydroamination (2014)

Figure 2. Catalytic cycle of intramolecular hydroamination proposed by Knowles *et al.*[36] This reaction proceeds at 85% yield in MeOH solvent.

METHODOLOGY

Combination of catalyst/substrate behaviors

Conceptual diagrams of our proposed method are shown in **Figures 3a–3c**. **Figure 3a** depicts a schematic potential energy profile of the paths from the reactant to the product, in both the S_0 state and the electronic doublet state of cation species for the substrate generated by oxidation *via* SET (denoted by D_0^{cation} or simply D_0). D_0^{cation} has a higher energy because it has one fewer electron than the substrate in the ground state (S_0). This reaction does not proceed on S_0 because of the high energy barrier along the reaction path. **Figure 3b** illustrates the three electronic states of the catalyst with stable structures (S_0, T_1, and D_0^{anion}), and the energy gaps between these states are related to redox potentials of the catalyst. This study uses the experimentally measured values of T_1–D_0^{anion} = 490.3 kJ/mol ($E_{1/2}$ = 0.66 V *vs*. SCE) and S_0–D_0^{anion} = 281.0 kJ/mol ($E_{1/2}$ = −1.51 V *vs*. SCE) as the oxidation and reduction potentials of [Ir(ppy)$_2$(dtbbpy)]PF$_6$ under the reductive quenching cycle.[33] **Figure 3c** combines the diagrams of **3a** and **3b** to show the reaction paths on three states: S_0 substrate and T_1 catalyst (denoted by S_0+T_1), D_0^{cation} substrate and D_0^{anion} catalyst

(D_0^{cation}+D_0^{anion} or simply D_0+D_0), and S_0 substrate and S_0 catalyst (S_0+S_0). The purple dash curve in **Figure 3c** describes the experimentally expected reaction path.[36] Along this expected path, photoexcitation generates the T_1 state of the catalyst, while SET from the substrate generates the D_0^{cation} substrate. After bond formation in D_0^{cation}, the substrate returns to the ground state S_0 by SET and forms the product.
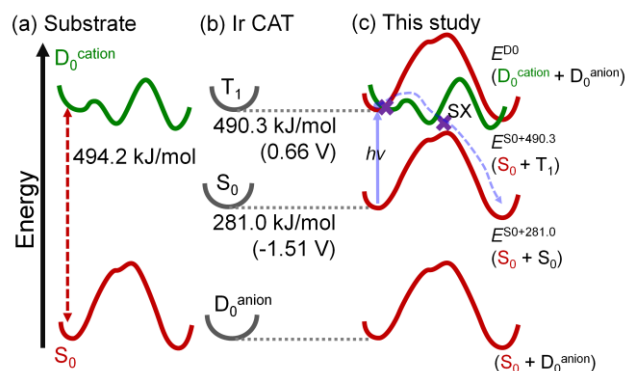

Figure 3. Schematic potential energy profiles representing the current method. (a) Potential energy profiles of the substrate along the reaction coordinate. (b) Energy levels of the electronic states corresponding to redox potentials of the photoredox catalyst. This study uses the experimentally measured values of the redox potential.[33] (c) Schematic energy profile in the proposed method. The purple dash curve corresponds to the expected reaction mechanism, and cross marks indicate the SXs.

The calculation model is described in **Figure 3c** based on the following three assumptions: 1) T_1 of the catalyst is generated immediately after photoexcitation to S_n, 2) there is no other interaction between the substrate and the catalyst except the SET, and 3) the substrate does not affect the redox potential of catalyst. Under these assumptions, the energies of the three states, S_0+T_1, D_0+D_0, and S_0+S_0, are calculated using the following equations:

$$E^{S0+T1} = E^{S0} + 490.3 \text{ kJ/mol} = E^{S0+490.3}$$

$$E^{D0+D0} = E^{D0} + 0.0 \text{ kJ/mol} = E^{D0}$$

$$E^{S0+S0} = E^{S0} + 281.0 \text{ kJ/mol} = E^{S0+281.0}$$

where E^{S0}, E^{D0}, E^{S0+T1}, E^{D0+D0}, and E^{S0+S0} correspond to the S_0 energy of the substrate, D_0^{cation} energy of the substrate, and energies of S_0+T_1, D_0+D_0, and S_0+S_0, respectively. $E^{S0+490.3}$ and $E^{S0+281.0}$ represent E^{S0}+490.3 kJ/mol and E^{S0}+281.0 kJ/mol, respectively. Shifting the energy by adding a constant value is equivalent to the energy shift (ES) method described in previous studies.[38,39] The ES method was originally developed to analyze the non-radiative decay path from the $4f^N$ excited state of lanthanide complexes. It dramatically reduces computational costs by avoiding explicit consideration of the catalyst. Additionally, this method allows us to approximate the potential energy surfaces involving three electronic states by using simple electronic structure calculations of the ground states (S_0 and D_0^{cation} of the substrate).

Exploration of reaction paths

The reaction path search in this study consists of three individual calculations for different processes: a reaction process considering the SET process between S_0+T_1 and D_0+D_0, a decay process from D_0+D_0 to S_0+S_0, and a process leading to products after the decay.

For the SET process of S_0+T_1 and D_0+D_0, the two states are assumed to be switched around the SX region, and the molecule should stay in the lower energy state. The avoided model function (AMF) approach[40] is useful for computing the lower state among two electronic states when the lower one is unknown in advance. In the AMF approach, the SX region of the potential energy surfaces is handled smoothly using the following formula:

$$F^{AMF}(\mathbf{Q}) = \frac{1}{2}\left(E^X(\mathbf{Q}) - E^Y(\mathbf{Q})\right) + \frac{1}{2}\sqrt{\left(E^X(\mathbf{Q}) - E^Y(\mathbf{Q})\right)^2 + 4U(\mathbf{Q})}$$

U is defined by the following equation:

$$U(\mathbf{Q}) = \frac{\beta}{2}\exp\left[-\kappa\left(\frac{E^X(\mathbf{Q}) - E^Y(\mathbf{Q})}{\beta}\right)^2\right]$$

where $\beta = 30.0$ kJ/mol and $\kappa = 0.10$.

The mechanism of the deactivation process from D_0+D_0 to S_0+S_0 was examined by finding the non-radiation decay path through the SX regions, namely calculating the minimum energy seam of crossing (MESX) between D_0+D_0 and S_0+S_0. However, it is not easy to estimate the MESX geometries, which prevents one from determining the energetically most favorable decay paths. Thus, we used automated exploration of MESX geometries in this stage. Specifically, we systematically explored the conformation of MESX based on the crossing search using the gradient projection (GP)/single component-artificial force induced reaction (SC-AFIR) method and the conventional SC-AFIR method.[30] The GP/SC-AFIR MESX search allows us to investigate the decay paths without prior knowledge of the molecular geometries. After obtaining the MESX geometries, the steepest descent path (meta-IRC) calculations provide the reaction path leading to the products from MESXs in S_0+S_0.

Computational details

In the target hydroamination reaction, experiments using MeOD solvent showed that deuterium (D) is fully incorporated at the benzylic position of the product.[36] Since MeOH, a solvent in this reaction, works as a proton source, we used a molecular model that explicitly considers two methanol molecules. In addition, all density functional theory (DFT) calculations incorporated the effect of MeOH by the implicit solvation SMD model.[41] Intramolecular hydroamination could form two possible types of five-membered-rings, **B** and **B'**, referred to as the *trans*- and *cis*-oriented cyclized product, respectively (**Figure 4c**). The reaction path exploration starts from each initial structure **A** (*trans* side and *cis* side). The initial structures were prepared by a conformational search in S_0 using the SC-AFIR method, and a structure with stable free energy was selected. Computational details of the search are described in **SI1**.

First, paths corresponding to the reaction processes at S_0+T_1 and D_0+D_0 were explored using AMF functions[40] and the SC-AFIR method (denoted by the ES/AMF/SC-AFIR method). The ωB97X-D functionals[42] and SV basis set were used (denoted by the ωB97X-D/SV level). Calculations at the ωB97X-D/SV level employed the Grid=fineGrid option. The target of the SC-AFIR search was set to nine atoms related to the reaction, *i.e.*, N_1, C_5, C_6, H_α, and H_β of the substrate (see structure A of **Figure 4c**) and two OH groups of methanol molecules. The model collision energy parameter, γ, was set to 100.0 kJ/mol. During the SC-AFIR search, the kinetic navigation method was employed to efficiently search for the kinetically

accessible geometries under the specified conditions.[43,44] Conditions of the kinetic simulations were set at 1.0 s and 200, 300, and 400 K, and the search using these settings explored the geometries by starting from the MINs accessible in the given reaction time (1.0 s). Details on kinetic navigation have been described in our previous reports.[43,44] The SC-AFIR searches terminated after computing 200 valid paths.

Reaction paths that contribute to the mechanism were re-optimized in D_0^{cation}, using a larger basis set of 6-311G(d,p), the default grid, and the ωB97X-D functional (denoted by the ωB97X-D/6-311G(d,p) level). The MESX between S_0+T_1 and D_0+D_0 (denoted by $D_0/S_{0+490.3}$-SX), which is related to the initial SET, was also optimized based on the most favorable path structure.

Next, the ES/GP/SC-AFIR method starting from the five-membered ring intermediate structures (the *trans* types) systematically explored the MESX geometries between D_0+D_0 and S_0+S_0 (denoted by $D_0/S_{0+281.0}$-SX), which correspond to paths of the SET process from the catalyst to substrate. In this MESX search, the ωB97X-D/SV level was used, and the SC-AFIR search targeted all atoms within the substrate. The model collision parameter, γ, was set to 100.0 kJ/mol in the search. Finally, all obtained structures were re-optimized at the ωB97X-D/6-311G(d,p) level to produce a list of MESX geometries.

The search results revealed low-energy $D_0/S_{0+281.0}$-SXs near the intermediate structure bearing a five-membered ring substructure in D_0^{cation}. Thus, we thoroughly searched for conformational isomers of $D_0/S_{0+281.0}$-SXs near this intermediate of both the *trans* and *cis* types. In the conformation search, the MIN structures in D_0^{cation} (D_{0MIN}) were explored using the SC-AFIR method at the ωB97X-D/SV level, and the obtained D_{0MIN} geometries were then optimized to the $D_0/S_{0+281.0}$-SXs at the ωB97X-D/6-311G(d,p) level. Connections to the decay paths were confirmed by steepest descent in the mass-weighted coordinates (meta-IRC) starting from the obtained $D_0/S_{0+281.0}$-SXs structures in the S_0 state at the ωB97X-D/6-311G(d,p) level. The computational details of the conformational search are described in **SI2** and **SI3**.

In addition, reaction paths for the SET from the Ir(II) complex to substrate in D_0 were investigated by calculating the MESX geometries between the T_1 state (Ir(II) complex with D_0-substrate) and the S_0 state (Ir(III) complex with S_0-substrate). These are denoted by T_1/S_0-SXs. In this study, T_1/S_0-SXs were optimized for the full system (141 atoms) including the substrate, two MeOHs, the catalyst, and its counter anion (PF_6^-). The orientations of three parts, i.e., the catalyst, PF_6^-, and the substrate with two MeOHs, were sampled by optimizing 200 random initial structures assuming T_1 in a vacuum at the GFN1-xTB level.[45,46] During the sampling, an additional harmonic potential prevented the geometry deformation within each part. Then, starting from the energetically most stable structure at the GFN1-xTB level, T_1/S_0-SX and the minimum of T_1 (denoted by T_{1MIN}) were optimized at the DFT level without the constrain. In the DFT calculations, the ωB97X-D functional and Def2-SVP basis set were employed, while MeOH solvent was incorporated by the SMD model (denoted by the ωB97X-D/Def2-SVP level). From the optimized T_1/S_0-SX structure, meta-IRC calculation in the S_0 state confirmed the decay path after the SET.

DFT energies and gradients were computed using the Gaussian16 package.[47] GFN1-xTB energies and gradients

were calculated using the ORCA program package.[48] Optimizations of the minima and MESXs and the SC-AFIR explorations were carried out using a developmental version of the GRRM program.[26,49]

RESULTS AND DISCUSSION

The reaction path networks (**Figures 4a** and **4b**) starting from **A** (*trans* side) and **A** (*cis* side) were obtained by ES/AMF/SC-AFIR search at the ωB97X-D/SV level for the *trans* and *cis* types, respectively. A total of 229 MINs (393 paths) were obtained for the *trans* type and 241 MINs (433 paths) for the *cis* type. The key reaction pathways starting from **A** are depicted in **Figure 4c**, where the MIN and TS in D_0^{cation} had been optimized at the ωB97X-D/6-311G(d,p) level for energetically favorable paths in the network of **Figures 4a** and **4b**. In this calculation, the *trans*-oriented **B** was obtained as the most stable structure. Therefore, energies of D_0^{cation} are shown relative to the intermediate **B** in kJ/mol. Important molecular structures and their energies are listed in **SI4**.
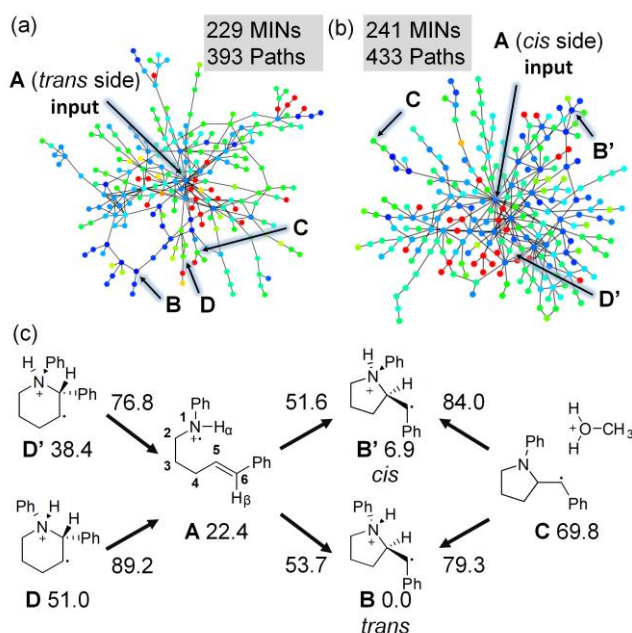

Figure 4. Reaction path networks calculated using the ES/AMF/SC-AFIR method at the ωB97X-D/SV level for (a) *trans*-type and (b) *cis*-type. Energies for the important reaction paths at the ωB97X-D/6-311G(d,p) level are shown relative to the most stable D_{0MIN} of intermediate **B** in kJ/mol.

The reaction path networks for both the *trans* and *cis* types include the experimentally observed five-membered ring formation path leading to **B** and **B'** as the preferable path, respectively. Paths leading to a six-membered ring (**D** and **D'**) are competing pathways. However, the TS energies for these paths are relatively high (89.2 and 76.8 kJ/mol, respectively), and **D** and **D'** also have higher energies than **A**. This selective formation of the five-membered cycle using this substrate is consistent with the fact that products containing the six-membered ring were not observed experimentally at all. In addition, paths to generate **C** have a high energy barrier because it is difficult for neutral MeOH to abstract proton from the intermediate structures **B** and **B'**. Although there are also some C–H and C–C bond dissociation paths in the reaction path network, their

very high reaction barriers indicate that they do not contribute to the process in D_0^{cation}.

Energy profile along the path from **A** to **B** is shown in **Figure 5**. All geometries along the path were optimized in D_0^{cation} using geometries obtained in the reaction path network, and the energies of D_0 and $S_{0+490.3}$ are indicated by green and red solid lines, respectively. Also, the cross mark indicates that optimization of $D_0/S_{0+490.3}$-SX (denoted by SX5a) started from a minimum of **A** in D_0 (25.8 kJ/mol). Meta-IRC calculations from SX5a in both D_0 and S_0 states lead to the reactant, indicating that the SET from the substrate to the catalyst, *i.e.*, decay from S_0+T_1 to D_0+D_0, occurs near the reactant region. Also, the TS energy for the five-membered ring formation (53.7 kJ/mol) is higher than the energy of SX5a (44.7 kJ/mol) and expected to make a larger contribution to the reaction rate than the SET process from the substrate to the catalyst. Furthermore, there is no energetically preferred reaction path to reach the product in D_0^{cation}. Therefore, the substrate is expected to stay in structure **B** during the reaction process and receives an electron from the catalyst around **B**.
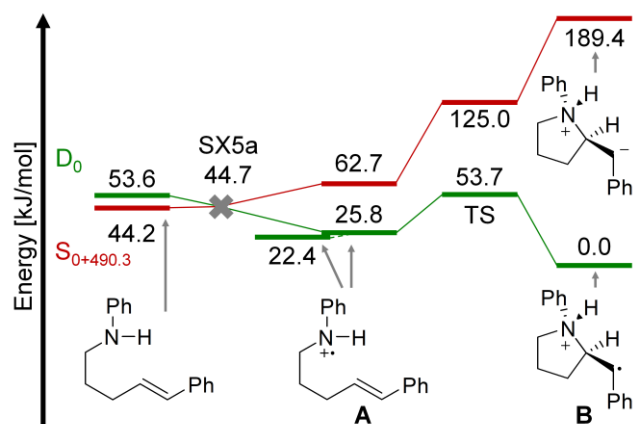

Figure 5. Energy profile of *trans* isomers at the ωB97X-D/6-311G(d,p) level. Thick green and red solid lines indicate the energies of D_0 and $S_{0+490.3}$, respectively. The cross mark indicates the $S_{0+490.3}/D_0$-SX, SX5a. IRC and meta-IRC paths are indicated by thin solid lines. Energies are given in kJ/mol relative to the most stable D_{0MIN} of intermediate **B**. The molecular structures and energies are shown in **SI4**.

The MESX search using the ES/GP/SC-AFIR method starting from **B** resulted in 71 $D_0/S_{0+281.0}$-SX structures, some of which are displayed in **Figure 6**. The structures are classified based on their bonding patterns, and the 16 energetically most favorable $D_0/S_{0+281.0}$-SX groups are shown by the lowest energy one. Note that the ES/GP/SC-AFIR method employs the FirstOnly option of the GRRM program[26,49] from structure **B**; hence, it may miss some MESXs in the same direction and some MESXs with more than two steps of geometry change from the original shape. All obtained crossing structures and their energies are shown in **SI5**.

Figure 6 shows that a stable $D_0/S_{0+281.0}$-SX, SX6a, exists in structure similar to intermediate **B** both structurally and energetically. Additionally, the search resulted in structures corresponding to the vicinity of the reactant **A** (SX6i), its proton transfer geometry (SX6j), and structures corresponding to **C** (SX6f) and the six-membered-ring structure **D** (SX6e). The list also includes MESXs involving C_5-H hydrogen transfer, such as SX6b. Notably, the existence of these SX regions indi-

cates possible SET processes from the catalyst to substrate. In other words, the MESX search provided us with decay paths related to the SET processes.
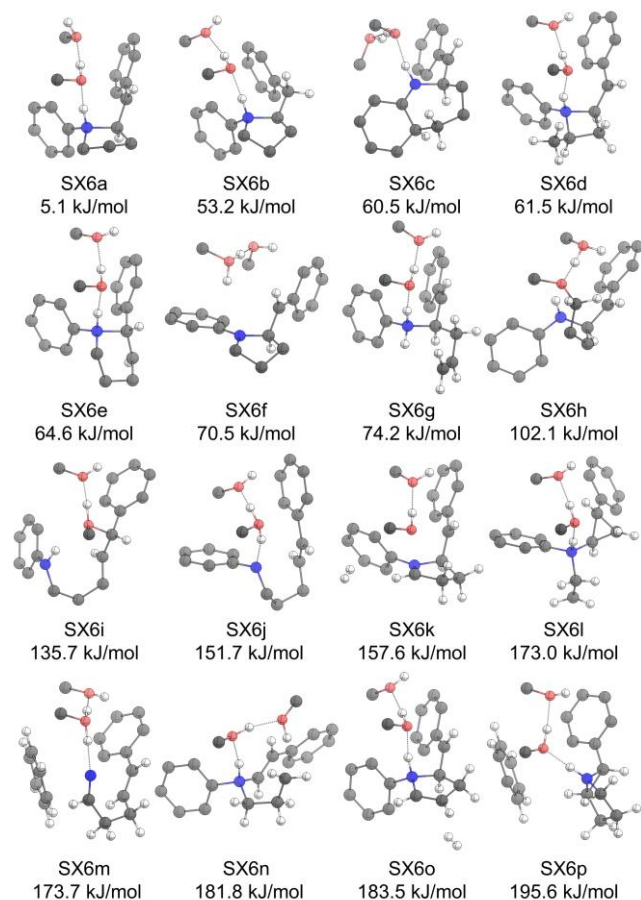

SX6a
5.1 kJ/mol

SX6b
53.2 kJ/mol

SX6c
60.5 kJ/mol

SX6d
61.5 kJ/mol

SX6e
64.6 kJ/mol

SX6f
70.5 kJ/mol

SX6g
74.2 kJ/mol

SX6h
102.1 kJ/mol

SX6i
135.7 kJ/mol

SX6j
151.7 kJ/mol

SX6k
157.6 kJ/mol

SX6l
173.0 kJ/mol

SX6m
173.7 kJ/mol

SX6n
181.8 kJ/mol

SX6o
183.5 kJ/mol

SX6p
195.6 kJ/mol

Figure 6. $D_0/S_{0+281.0}$-SX structures obtained by the ES/GP/SC-AFIR method. The structures were classified by bonding patterns, and the 16 most stable groups are shown with the lowest energy geometry for each group. Energies are given in kJ/mol relative to the most stable D_{0MIN} of intermediate **B**. All obtained MESX geometries and energies are shown in **SI5**.

A comparison of these MESXs reveals that one MESX structure similar to intermediate **B** (SX6a) is about 50 kJ/mol more stable than the other MESXs. Therefore, the SX6a structure plays an important role in the reduction process of the substrate. Thus, the conformational isomers were thoroughly explored to investigate the energetically favorable SX structure.

Conformational geometry search in the vicinity of structures **B** and **B'** provided 445 $D_0/S_{0+281.0}$-SX structures at the ωB97X-D/6-311G(d,p) level. Among them, 436 had the same bonding pattern as the reaction intermediates **B** and **B'**. All obtained molecular structures and their energies are shown in **SI6**. From all obtained $D_0/S_{0+281.0}$-SX structures, meta-IRC in S_0 was computed, and the $D_0/S_{0+281.0}$-SX structures were classified into the following three types: those going back to the reactant side (379/436), those forming ammonium ion intermediate **B** or **B'** in the S_0 state (51/436), and those leading directly to products (6/436). These calculations confirmed the presence of local minima of the ammonium intermediate **B** in S_0. Additionally, MESXs leading to the products are very rare in the list of obtained MESXs (6/436 = 1.4%). Therefore, a thorough

exploration of MESXs is essential to find the decay path corresponding to the experimentally suggested reaction paths.

Figure 7a depicts the most stable D_{0MIN} structure obtained in calculations. **Figure 7b** illustrates the $D_0/S_{0+281.0}$-SX that is structurally close to the most stable D_{0MIN}. The most stable $D_0/S_{0+281.0}$-SXs of the three types (leading to the reactant, intermediate **B** in S_0, and the product) are shown in **Figures 7c, 7d**, and **7e**. Since SX7b to SX7e are all *trans* types, the *cis*-type lowest $D_0/S_{0+281.0}$-SX structure is additionally shown in **Figure 7f**.
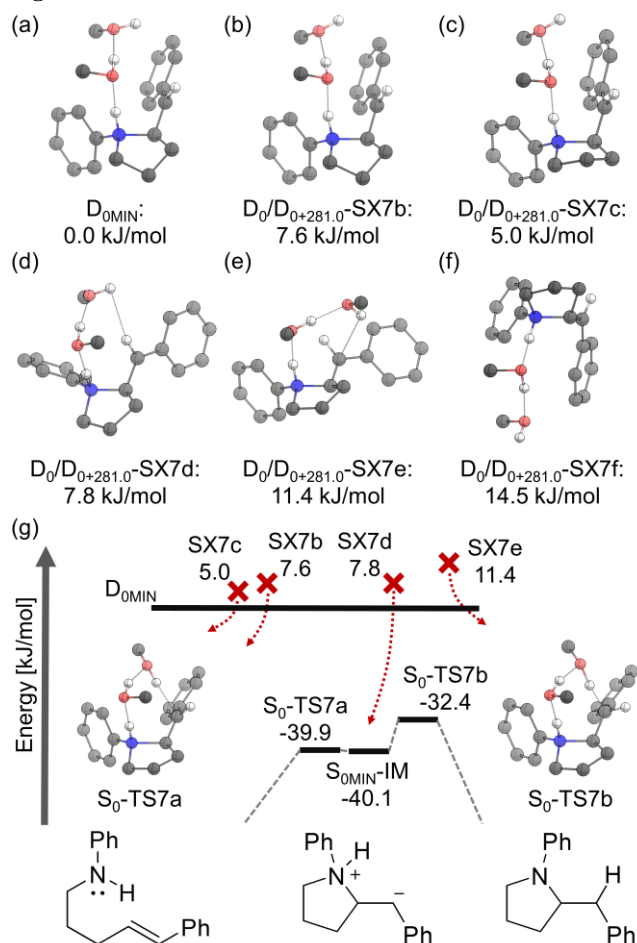

(a)

D_{0MIN}:
0.0 kJ/mol

(b)

$D_0/D_{0+281.0}$-SX7b:
7.6 kJ/mol

(c)

$D_0/D_{0+281.0}$-SX7c:
5.0 kJ/mol

(d)

$D_0/D_{0+281.0}$-SX7d:
7.8 kJ/mol

(e)

$D_0/D_{0+281.0}$-SX7e:
11.4 kJ/mol

(f)

$D_0/D_{0+281.0}$-SX7f:
14.5 kJ/mol

(g)

Figure 7. (a) The most stable D_{0MIN} geometry of the intermediate **B**. (b) SX7b: the MESX near the most stable geometry. (c) SX7c: the lowest MESX leading to the reactant. (d) SX7d: the lowest MESX leading to intermediate **B** in S_0. (e) SX7e: the lowest MESX leading to the product. (f) SX7f: the lowest MESX of *cis*-type. (g) Schematic potential energy profile around the intermediate structure. Energies are given in kJ/mol relative to the most stable D_{0MIN} of intermediate **B**.

Analysis focusing on $D_0/S_{0+281.0}$-SX geometries leading to the product (6/436 within the group of SX7e) revealed that they share a common molecular structure where the phenyl group is twisting to the outside, as shown in **Figure 7e**. SX7e is less stable than the two most stable $D_0/S_{0+281.0}$-SXs (SX7b and SX7c) where two phenyl groups face each other, as shown in **Figures 7b** and **7c**. The six $D_0/S_{0+281.0}$-SX geometries within the group of SX7e have a hydrogen bond network among the N_1-H, C_6, and two -OH groups of methanol, as shown in **Figure 7e**. The formation of a hydrogen bond network allows the meta-IRC paths in S_0 to directly lead to the product.

As shown in **Figure 7d**, the $D_0/S_{0+281.0}$-SX leading to intermediate **B** in S_0, SX7d, also has the twisting phenyl group geometry like SX7e. However, the two MeOH configurations in SX7d do not form the hydrogen bond network that is necessary to reach the product. **Figure 7g** depicts two TS structures and energies from intermediate **B** in S_0 to reactants and products: the path S_0-TSa leading to the reactant side has a lower reaction barrier than that to the product side (S_0-TSb). Hence, SX7d is expected to yield the reaction product less frequently. Notably, there are several *cis*-type $D_0/S_{0+281.0}$-SXs leading to intermediate **B'** in S_0. However, the *cis*-type $D_0/S_{0+281.0}$-SX, *e.g.*, SX7f in **Figure 7f**, is relatively unstable and would not contribute to the reaction process.

The present method expresses the redox potential of the catalyst by its energy shift value (V_{ES}), which allows easy extension to different catalysts. **Figure 8** plots the variation of D_0/S_{0+VES}-SX energies against V_{ES} for the four structures (SX7b, SX7c, SX7e, and SX7f) indicated by black circles, red triangles, orange cross marks, and blue squares, respectively. Since the energies are shown relative to the most stable D_{0MIN} (**Figure 7a**), the lowest point of the black line for the MESX near D_{0MIN}, *i.e.*, SX7b, is almost at zero.
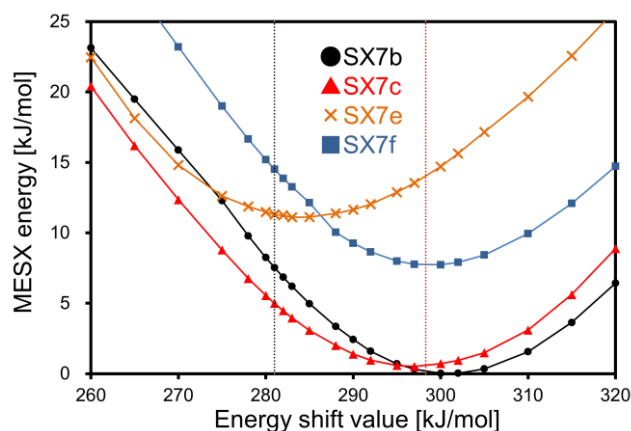

Figure 8. Dependence of MESX energies on the energy shift value (V_{ES}). The V_{ES} value corresponding to the reduction potential of the catalyst is plotted on the *x*-axis, and the energy of D_0/S_{0+VES}-SX is plotted on the *y*-axis relative to the most stable D_{0MIN} of intermediate **B**. The four lines correspond to four MESXs (SX7b, SX7c, SX7e, and SX7f) in **Figure 7**. Black and red vertical dotted lines correspond to $V_{ES} = 281.0$ kJ/mol (–1.51 V *vs*. SCE) and 298.3 kJ/mol (–1.33 V *vs*. SCE), respectively.

As shown in **Figure 8**, the MESX energy takes a minimum value at a specific V_{ES} for each crossing. The existence of a minimum on the plot corresponds to the Marcus inverted region.[22] In other words, specific energy matching is important for lowering the barrier of the SET path. As shown in **Figure 8**, the shift value that provides a low MESX energy depends on the type of $D_0/S_{0+281.0}$-SX. In particular, SX7e leading to the product (orange cross marks) reaches the minimum at around 283 kJ/mol, which is different from the other three cases of SX7b, SX7c, and SX7f. These four geometries have the same bonding pattern, and the small geometrical difference lies in their conformation. Thus, **Figure 8** suggests that a change in the redox potential can affect the relative stability of the SET path (MESX energy).

The experimental reaction yields[36] measured by gas chromatography were 43% with the Ru catalyst (298.3 kJ/mol, –1.33 V *vs*. SCE) and 88% with the Ir catalyst (281.0 kJ/mol, –

1.51 V *vs*. SCE). The corresponding redox potentials are indicated by red and black vertical dotted lines, respectively. In fact, the photoinduced SET is affected by various factors including counter anions of the Ir catalyst, reaction time, and employed solvents. Thus, the difference in redox potential alone does not necessarily explain the reaction yields. On the other hand, calculations showed that the energy of SX7e relative to SX7b or SX7c is lower at $V_{ES} = 281.0$ kJ/mol (Ir catalyst) than that at $V_{ES} = 298.3$ kJ/mol (Ru catalyst) in **Figure 8**. In other words, when using the Ir catalyst ($V_{ES} = 281.0$ kJ/mol), the SX leading to the product (SX7e, orange cross marks) is stabilized relative to the other MESXs. These results may explain the experimental observation that the Ir catalyst led to a high yield. Notably, in this discussion, the difference in the suitable V_{ES} for conformationally different MESX geometries may be a key factor in controlling the activity of the target reaction by selecting the photoredox.

Finally, the reliability of the ES approach was investigated by calculating MESXs of the system using the explicit catalyst. The MESX geometries between the T_1 (Ir(II) complex with the D_0-substrate) and the S_0 state (Ir(III) complex with the S_0-substrate) were calculated for a large system of 141 atoms including the substrate, two MeOHs, the catalyst, and PF_6^-. The optimization started from the energetically favorable $D_0/S_{0+281.0}$-SXs, *i.e.*, SX7c and SX7e. As a result, T_1/S_0-SXs were easily optimized using the proposed method, and the results are shown in **Figures 9a** and **9b** for SX7c and SX7e, respectively. The energy is shown relative to T_{1MIN} at relatively lower energy among the geometry optimized from these two T_1/S_0-SXs.
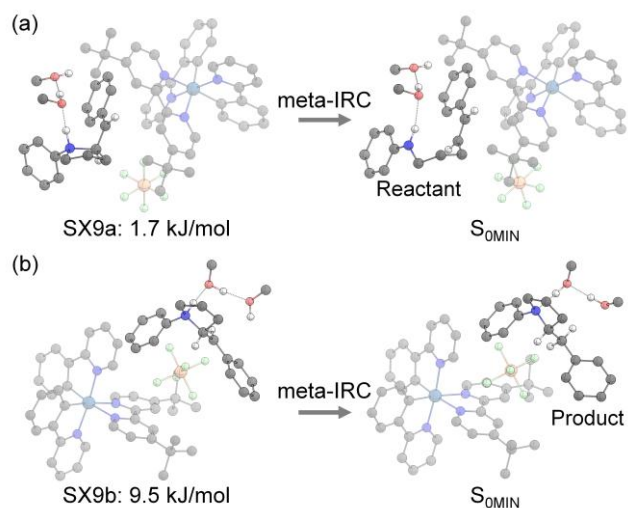

Figure 9. MESXs between T_1 and S_0 (T_1/S_0-SXs) and the terminal point of meta-IRC paths in S_0 starting from them at the ωB97X-D/Def2-SVP level. (a) SX9a is for the most stable $D_0/S_{0+281.0}$-SX (SX7c) and (b) SX9b is for the most stable $D_0/S_{0+281.0}$-SX leading to the product (SX7e) shown in **Figure 7**. Energies are given in kJ/mol relative to one of the optimized T_{1MIN}.

As shown in **Figures 9a** and **9b**, the meta-IRC path in S_0 from T_1/S_0-SXs (*i.e.*, SX9a and SX9b) led to the reactant and product sides, respectively, the same as the results calculated without catalysts. This agreement proves that results obtained using the present ES method represent the SET mechanism of the system including the explicit catalyst. The coordination structure searches were carried out at the GFN1-xTB level, but the obtained structure was not the most stable one at the DFT

level. Therefore, in this study we did not compare the energies of these two crossing structures. Notably, finding the T_1/S_0-SX structure leading to this product requires an exhaustive search for T_1/S_0-SX, which is computationally impractical. In contrast, the present approach based on the ES method realized the MESX search and allowed us to find the decay path (the SET path) to the product in the target system.

The present mechanism and the previously proposed one are compared in **Figures 10a** and **10b**. Previous studies indicated that the reduction and protonation processes occurred sequentially, *i.e.*, in a step-wise mechanism (**Figure 10a**). However, in the present calculations the five-membered ring intermediate structure was unstable in S_0. Additionally, the meta-IRC in S_0 from SX9b lead directly to the product minimum, as shown in **Figure 9b**. This result indicates a competitive reaction process, in which the protonation process and the reduction process by SET proceed simultaneously (**Figure 10b**). In other words, the present calculation suggests a concerted mechanism of the reduction and protonation processes.
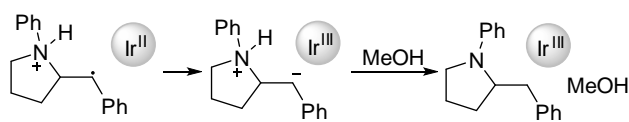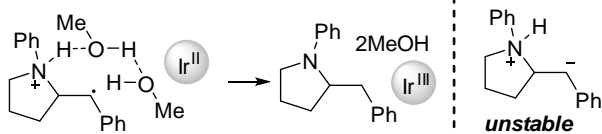

Figure 10. Schematics of reaction mechanisms (a) proposed in the literature[36] and (b) based on the computational results here.
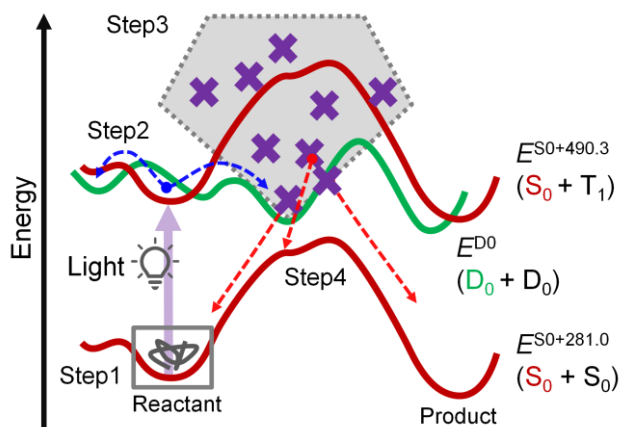

Figure 11. Entire scheme of the present approach. Step 1: preparation of the reactant geometry in S_0. Step 2: systematic exploration of the reaction paths using the ES/AMF/SC-AFIR method from the reactant. Step 3: MESX search around the obtained intermediate. Step 4: meta-IRC in S_0 calculated from the obtained MESXs.

Finally, the entire scheme for analyzing the target reaction is illustrated in **Figure 11**. Step 1 prepares the reactant geometry. Step 2 performs systematic exploration of the ES/AMF/SC-AFIR search with the kinetic navigation method, which provides us with possible intermediate species in the

generated cation of the substrate. Step 3 systematically explores MESXs corresponding to the SET path from the catalyst to the products. Finally, Step 4 calculates the meta-IRC paths in S_0 from the obtained MESXs, providing us with the decay path leading to the product after the SET. This scheme automates the analysis of the entire reaction mechanism of the target reaction, including the SET between the catalyst and substrate and bond reorganization in the substrate.

CONCLUSIONS

In this study, systematic reaction path exploration based on quantum chemical calculations revealed the entire complex reaction mechanism of photoredox-catalyzed Knowles's intramolecular hydroamination. There are three competing processes: 1) oxidation of the substrate with SET from the substrate to the catalyst; 2) reaction process involving ring formation of the oxidized radical cation substrate; 3) the protonation process promoted by MeOH, with the simultaneous reduction of the substrate by SET from the catalyst. In the actual calculation, the conventional reaction path search method was used to investigate reaction mechanisms involving bond-formation/cleavage processes, while systematic MESX exploration found the path for the SET between the catalyst and substrate. The obtained reaction mechanism along the energetically most favorable path is almost consistent with the experimentally proposed one. However, the present calculations showed that the protonation process occurs simultaneous to the reduction process of SET from the catalyst to substrate. Furthermore, systematic exploration of the MESX structures showed that conformational isomers near the intermediate structure play a key role in the path leading to the product.

The analyses were enabled by a new approach using the ES method, in which the photoredox catalyst is replaced by its redox potentials in the calculation. This permits the systematic search for MESXs, which is not practical when explicitly considering the Ir complex catalyst and PF_6^- with 92 atoms. The method also allowed us to express the redox potential of the complex by a simple ES value (V_{ES}). The variation of MESX energy against V_{ES} suggests that the suitable redox potential is different between the SET paths *via* MESXs leading to the product and reactant. This difference in suitable V_{ES} may be a key in controlling the reactivity of the target reaction by selecting the photoredox catalyst.

The advantage of the present approach is that all electronic state calculations are done using ground-state DFT calculations. Furthermore, the method is applicable to SET processes catalyzed by metal complexes and molecules of any size and any elemental composition, since the catalyst is not explicitly included in the calculation. Therefore, we believe that this approach is promising for the theoretical screening of photoredox catalysts. Additionally, the relationship between redox potential and electron transfer efficiency provides a design guideline for photoredox-catalyzed radical reactions.

ASSOCIATED CONTENT

Computational details of the conformation search (PDF), and the list of MIN, TS and SX geometries (xyz files).

AUTHOR INFORMATION

Corresponding Authors

Yu Harabuchi: y_harabuchi@sci.hokudai.ac.jp

Satoshi Maeda: smaeda@eis.hokudai.ac.jp

Notes

ACKNOWLEDGMENTS

ABBREVIATIONS

MESX, minimum energy seam of crossing; AFIR method, artificial force induced reaction method.

REFERENCES

(1) Houk, K. N.; Liu, F. Holy Grails for Computational Organic Chemistry and Biochemistry. *Acc. Chem. Res.* **2017**, *50*, 539–543.

(2) Nørskov, J. K.; Bligaard, T.; Rossmeisl, J.; Christensen, C. H. Towards the Computational Design of Solid Catalysts. *Nat. Chem.* **2009**, *1*, 37–46.

(3) Thiel, W. Computational Catalysis-Past, Present, and Future. *Angew. Chem. Int. Ed.* **2014**, *53*, 8605–8613.

(4) Sameera, W. M. C.; Maeda, S.; Morokuma, K. Computational Catalysis Using the Artificial Force Induced Reaction Method. *Acc. Chem. Res.* **2016**, *49*, 763–773.

(5) Ahn, S.; Hong, M.; Sundararajan, M.; Ess, D. H.; Baik, M.-H. Design and Optimization of Catalysts Based on Mechanistic Insights Derived from Quantum Chemical Reaction Modeling. *Chem. Rev.* **2019**, *119*, 6509–6560.

(6) Dewyer, A. L.; Argüelles, A. J.; Zimmerman, P. M. Methods for Exploring Reaction Space in Molecular Systems: Exploring Reaction Space in Molecular Systems. *WIREs Comput. Mol. Sci.* **2018**, *8*, e1354.

(7) Simm, G. N.; Vaucher, A. C.; Reiher, M. Exploration of Reaction Pathways and Chemical Transformation Networks. *J. Phys. Chem. A* **2019**, *123*, 385–399.

(8) Sumiya, Y.; Maeda, S. Paths of Chemical Reactions and Their Networks: From Geometry Optimization to Automated Search and Systematic Analysis. In *Chemical Modelling*; Springborg, M., Joswig, J.-O., Eds.; Royal Society of Chemistry: Cambridge, 2019; Vol. 15, pp 28–69.

(9) Nicewicz, D. A.; MacMillan, D. W. C. Merging Photoredox Catalysis with Organocatalysis: The Direct Asymmetric Alkylation of Aldehydes. *Science* **2008**, *322*, 77–80.

(10) Shaw, M. H.; Twilton, J.; MacMillan, D. W. C. Photoredox Catalysis in Organic Chemistry. *J. Org. Chem.* **2016**, *81*, 6898–6926.

(11) Fernandez-Alvarez, V. M.; Maseras, F. Computational Characterization of the Mechanism for the Light-Driven Catalytic Trichloromethylation of Acylpyridines. *Org. Biomol. Chem.* **2017**, *15*, 8641–8647.

(12) Funes-Ardoiz, I.; Garrido-Barros, P.; Llobet, A.; Maseras, F. Single Electron Transfer Steps in Water Oxidation Catalysis. Redefining the Mechanistic Scenario. *ACS Catal.* **2017**, *7*, 1712–1719.

(13) Qi, Z.-H.; Ma, J. Dual Role of a Photocatalyst: Generation of Ni(0) Catalyst and Promotion of Catalytic C–N Bond Formation. *ACS Catal.* **2018**, *8*, 1456–1463.

(14) de Aguirre, A.; Funes-Ardoiz, I.; Maseras, F. Computational Characterization of Single-Electron Transfer Steps in Water Oxidation. *Inorganics* **2019**, *7*, 32.

(15) Dong, Y.-J.; Zhu, B.; Geng, Y.; Zhao, Z.-W.; Su, Z.-M.; Guan, W. Radical Mechanism of Ir^{III}/Ni^{II}-Metallaphotoredox-Catalyzed C(sp^3)–H Functionalization Triggered by Proton-Coupled Electron Transfer: Theoretical Insight. *CCS Chem.* **2022**, *4*, 1429–1440.

(16) Koga, N.; Morokuma, K. Determination of the Lowest Energy Point on the Crossing Seam Between Two Potential Surfaces Using the Energy Gradient. *Chem. Phys. Lett.* **1985**, *119*, 371–374.

(17) Bernardi, F.; Olivucci, M.; Robb, M. A. Potential Energy Surface Crossings in Organic Photochemistry. *Chem. Soc. Rev.* **1996**, *25*, 321.

(18) Yarkony, D. R. Diabolical Conical Intersections. *Rev. Mod. Phys.* **1996**, *68*, 985–1013.

(19) Yarkony, D. R. Conical Intersections: Diabolical and Often Misunderstood. *Acc. Chem. Res.* **1998**, *31*, 511–518.

(20) Sobolewski, A. L.; Domcke, W.; Dedonder-Lardeux, C.; Jouvet, C. Excited-State Hydrogen Detachment and Hydrogen Transfer Driven by Repulsive $^1\pi\sigma*$ States: A New Paradigm for Nonradiative Decay in Aromatic Biomolecules. *Phys. Chem. Chem. Phys.* **2002**, *4*, 1093–1100.

(21) Nanbu, S.; Ishida, T.; Nakamura, H. Future Perspectives of Nonadiabatic Chemical Dynamics. *Chem. Sci.* **2010**, *1*, 663.

(22) Marcus, R. A. On the Theory of Oxidation-Reduction Reactions Involving Electron Transfer. I. *J. Chem. Phys.* **1956**, *24*, 966–978.

(23) Marcus, R. A. Electron Transfer Reactions in Chemistry: Theory and Experiment (Nobel Lecture). *Angew. Chem. Int. Ed. Engl.* **1993**, *32*, 1111–1121.

(24) Uematsu, R.; Saka, C.; Sumiya, Y.; Ichino, T.; Taketsugu, T.; Maeda, S. An Autocatalytic Cycle in Autoxidation of Triethylborane. *Chem. Commun.* **2017**, *53*, 7302–7305.

(25) Maeda, S.; Ohno, K.; Morokuma, K. Systematic Exploration of the Mechanism of Chemical Reactions: The Global Reaction Route Mapping (GRRM) Strategy Using the ADDF and AFIR Methods. *Phys. Chem. Chem. Phys.* **2013**, *15*, 3683.

(26) Maeda, S.; Harabuchi, Y. Exploring Paths of Chemical Transformations in Molecular and Periodic Systems: An Approach Utilizing Force. *WIREs Comput. Mol. Sci.* **2021**, *11*, e1538.

(27) Sumiya, Y.; Harabuchi, Y.; Nagata, Y.; Maeda, S. Quantum Chemical Calculations to Trace Back Reaction Paths for the Prediction of Reactants. *JACS Au* **2022**, *2*, 1181–1188.

(28) Mita, T.; Harabuchi, Y.; Maeda, S. Discovery of a Synthesis Method for a Difluoroglycine Derivative Based on a Path Generated by Quantum Chemical Calculations. *Chem. Sci.* **2020**, *11*, 7569–7577.

(29) Maeda, S.; Harabuchi, Y.; Taketsugu, T.; Morokuma, K. Systematic Exploration of Minimum Energy Conical Intersection Structures near the Franck–Condon Region. *J. Phys. Chem. A* **2014**, *118*, 12050–12058.

(30) Harabuchi, Y.; Taketsugu, T.; Maeda, S. Combined Gradient Projection/Single Component Artificial Force Induced Reaction (GP/SC-AFIR) Method for an Efficient Search of Minimum Energy Conical Intersection (MECI) Geometries. *Chem. Phys. Lett.* **2017**, *674*, 141–145.

(31) Harabuchi, Y.; Taketsugu, T.; Maeda, S. Exploration of Minimum Energy Conical Intersection Structures of Small Polycyclic Aromatic Hydrocarbons: Toward an Understanding of the Size Dependence of Fluorescence Quantum Yields. *Phys. Chem. Chem. Phys.* **2015**, *17*, 22561–22565.

(32) Saita, K.; Harabuchi, Y.; Taketsugu, T.; Ishitani, O.; Maeda, S. Theoretical Study on Mechanism of the Photochemical Ligand Substitution of *fac*-[Re^I(Bpy)(CO)$_3$(PR$_3$)]$^+$ Complex. *Phys. Chem. Chem. Phys.* **2016**, *18*, 17557–17564.

(33) Lowry, M. S.; Goldsmith, J. I.; Slinker, J. D.; Rohl, R.; Pascal, R. A.; Malliaras, G. G.; Bernhard, S. Single-Layer Electrolumines-

cent Devices and Photoinduced Hydrogen Production from an Ionic Iridium(III) Complex. *Chem. Mater.* **2005**, *17*, 5712–5719.

(34) Maeda, S.; Morokuma, K. Finding Reaction Pathways of Type A + B → X: Toward Systematic Prediction of Reaction Mechanisms. *J. Chem. Theory Comput.* **2011**, *7*, 2335–2345.

(35) Maeda, S.; Taketsugu, T.; Morokuma, K. Exploring Transition State Structures for Intramolecular Pathways by the Artificial Force Induced Reaction Method. *J. Comput. Chem.* **2014**, *35*, 166–173.

(36) Musacchio, A. J.; Nguyen, L. Q.; Beard, G. H.; Knowles, R. R. Catalytic Olefin Hydroamination with Aminium Radical Cations: A Photoredox Method for Direct C–N Bond Formation. *J. Am. Chem. Soc.* **2014**, *136*, 12217–12220.

(37) Ganley, J. M.; Murray, P. R. D.; Knowles, R. R. Photocatalytic Generation of Aminium Radical Cations for C–N Bond Formation. *ACS Catal.* **2020**, *10*, 11712–11738.

(38) Hatanaka, M.; Morokuma, K. Exploring the Reaction Coordinates for f–f Emission and Quenching of Lanthanide Complexes – Thermosensitivity of Terbium(III) Luminescence. *J. Chem. Theory Comput.* **2014**, *10*, 4184–4188.

(39) Hatanaka, M.; Hirai, Y.; Kitagawa, Y.; Nakanishi, T.; Hasegawa, Y.; Morokuma, K. Organic Linkers Control the Thermosensitivity of the Emission Intensities from Tb(III) and Eu(III) in a Chameleon Polymer. *Chem. Sci.* **2017**, *8*, 423–429.

(40) Maeda, S.; Ohno, K.; Morokuma, K. Exploring Multiple Potential Energy Surfaces: Photochemistry of Small Carbonyl Compounds. *Adv. Phys. Chem.* **2012**, *2012*, 1–13.

(41) Marenich, A. V.; Cramer, C. J.; Truhlar, D. G. Universal Solvation Model Based on Solute Electron Density and on a Continuum Model of the Solvent Defined by the Bulk Dielectric Constant and Atomic Surface Tensions. *J. Phys. Chem. B* **2009**, *113*, 6378–6396.

(42) Chai, J.-D.; Head-Gordon, M. Long-Range Corrected Hybrid Density Functionals with Damped Atom-Atom Dispersion Corrections. *Phys. Chem. Chem. Phys.* **2008**, *10*, 6615–6620.

(43) Sumiya, Y.; Maeda, S. A Reaction Path Network for Wöhler's Urea Synthesis. *Chem. Lett.* **2019**, *48*, 47–50.

(44) Sumiya, Y.; Maeda, S. Rate Constant Matrix Contraction Method for Systematic Analysis of Reaction Path Networks. *Chem. Lett.* **2020**, *49*, 553–564.

(45) Grimme, S.; Bannwarth, C.; Shushkov, P. A Robust and Accurate Tight-Binding Quantum Chemical Method for Structures, Vibrational Frequencies, and Noncovalent Interactions of Large Molecular Systems Parametrized for All spd-Block Elements (*Z* = 1–86). *J. Chem. Theory Comput.* **2017**, *13*, 1989–2009.

(46) Bannwarth, C.; Caldeweyher, E.; Ehlert, S.; Hansen, A.; Pracht, P.; Seibert, J.; Spicher, S.; Grimme, S. Extended Tight-Binding Quantum Chemistry Methods. *WIREs Comput. Mol. Sci.* **2021**, *11*.

(47) Frisch, M. J.; Trucks, G. W.; Schlegel, H. B.; Scuseria, G. E.; Robb, M. A.; Cheeseman, J. R.; Scalmani, G.; Barone, V.; Petersson, G. A.; Nakatsuji, H.; Li, X.; Caricato, M.; Marenich, A. V.; Bloino, J.; Janesko, B. G.; Gomperts, R.; Mennucci, B.; Hratchian, H. P.; Ortiz, J. V.; Izmaylov, A. F.; Sonnenberg, J. L.; Williams; Ding, F.; Lipparini, F.; Egidi, F.; Goings, J.; Peng, B.; Petrone, A.; Henderson, T.; Ranasinghe, D.; Zakrzewski, V. G.; Gao, J.; Rega, N.; Zheng, G.; Liang, W.; Hada, M.; Ehara, M.; Toyota, K.; Fukuda, R.; Hasegawa, J.; Ishida, M.; Nakajima, T.; Honda, Y.; Kitao, O.; Nakai, H.; Vreven, T.; Throssell, K.; Montgomery Jr., J. A.; Peralta, J. E.; Ogliaro, F.; Bearpark, M. J.; Heyd, J. J.; Brothers, E. N.; Kudin, K. N.; Staroverov, V. N.; Keith, T. A.; Kobayashi, R.; Normand, J.; Raghavachari, K.; Rendell, A. P.; Burant, J. C.; Iyengar, S. S.; Tomasi, J.; Cossi, M.; Millam, J. M.; Klene, M.; Adamo, C.; Cammi, R.; Ochterski, J. W.; Martin, R. L.; Morokuma, K.; Farkas, O.; Foresman, J. B.; Fox, D. J. *Gaussian 16 Rev. C.01*; Wallingford, CT, 2016.

(48) Neese, F.; Wennmohs, F.; Becker, U.; Riplinger, C. The ORCA Quantum Chemistry Program Package. *J. Chem. Phys.* **2020**, *152*, 224108.

(49) Maeda, S.; Harabuchi, Y.; Takagi, M.; Saita, K.; Suzuki, K.; Ichino, T.; Sumiya, Y.; Sugiyama, K.; Ono, Y. Implementation and Performance of the Artificial Force Induced Reaction Method in the GRRM17 Program. *J. Comput. Chem.* **2018**, *39*, 233–251.

TOC Graphics